

Article

Effect of Heat Treatment Process on the Optimization of Grain Boundary Character Distribution in Heavy Gage Austenitic Stainless Steel

Zhiguo Wang ¹, Weina Zhang ^{1,*}, Aoran Ma ², Jianyuan Li ², Fei Gao ^{2,*}, Chengang Li ¹ and Zhenyu Liu ¹¹ State Key Laboratory of Rolling and Automation, Northeastern University, Shenyang 110819, China² Key Laboratory of Lightweight Structural Materials, School of Materials Science and Engineering, Northeastern University, Shenyang 110819, China

* Correspondence: zhangwn@ral.neu.edu.cn (W.Z.); gaof@mail.neu.edu.cn (F.G.)

Abstract: The optimization of grain boundary character distribution (GBCD) is of great significance to improve the GB-related properties for heavy-gauge austenitic stainless steels worked in harsh environments such as reactors of nuclear power, which can usually be realized by regulating the thermomechanical process. In this paper, special solution annealing processes for a hot-rolled nuclear grade 316H plate were designed to introduce different character distribution of Σ^{3^n} boundaries ($1 \leq n \leq 3$) and random high-angle GBs (RHAGBs), and the regulation principle among them were clarified. It was worked out that the optimized GBCD by characterization of large twin related domains, abundant interconnected Σ^{3^n} boundaries and interrupted topology network of RHAGBs could be effectively facilitated through solution annealing with a long time period at lower temperature or short time period at higher temperature, in which the recrystallization, grain growth and GB migration during heat treatment process played key roles. Moreover, the length fraction of Σ^{3^n} boundaries were found to be hardly changed when they reached about 77%, but their character distribution could be continuously optimized.

Keywords: Σ^{3^n} boundaries; character distribution; recrystallization; annealing; stainless steel



Citation: Wang, Z.; Zhang, W.; Ma, A.; Li, J.; Gao, F.; Li, C.; Liu, Z. Effect of Heat Treatment Process on the Optimization of Grain Boundary Character Distribution in Heavy Gage Austenitic Stainless Steel. *Crystals* **2023**, *13*, 89. <https://doi.org/10.3390/cryst13010089>

Academic Editor: Pavel Lukáč

Received: 30 November 2022

Revised: 30 December 2022

Accepted: 31 December 2022

Published: 3 January 2023



Copyright: © 2023 by the authors. Licensee MDPI, Basel, Switzerland. This article is an open access article distributed under the terms and conditions of the Creative Commons Attribution (CC BY) license (<https://creativecommons.org/licenses/by/4.0/>).

1. Introduction

Benefiting from stable austenite structure and strictly controlled element content (Co, B etc.) with large neutron absorption section during service for providing the resistance against material embrittlement under the action of high neutron flux in nuclear reactor, austenitic stainless steels (ASSs) are often used in key structural parts and protective components in nuclear power systems [1,2], such as the 316H designated for main vessel and internal components in sodium-cooled fast reactors [3]. These ASSs usually have heavy-gauge and are fabricated through hot rolling followed by solution annealing, and the excellent comprehensive properties such as high temperature strength, creep, fatigue and intergranular corrosion (IGC) resistance are very critical to ensuring the safety and stability of key components during operation [4,5]. Moreover, due to strict requirements on the chemical composition of nuclear-grade materials, the regulation of microstructure during thermomechanical processes becomes particularly important to obtain excellent properties.

Numerous studies have indicated that optimizing grain boundary character distribution (GBCD) in a microstructure, i.e., increasing the frequency of low- Σ ($\Sigma \leq 29$) coincidence site lattice (CSL) boundaries (mainly Σ^{3^n} , $1 \leq n \leq 3$) and regulating their distribution [6–8], can dramatically improve the resistance to IGC [8–11], intergranular stress corrosion cracking [12,13] and hydrogen embrittlement [14,15], etc. Kobayashi et al. [16] found that by increasing the fraction of low- Σ CSL boundaries in a GB network, the propagation rate of cracks along random boundaries can be significantly weakened, and the embrittlement of

polycrystalline nickel can be effectively controlled, which can improve the crack arrest capability of the material and increase the safety in service. Moreover, Li and co-workers [17,18] worked out that the twin boundaries have an intrinsically higher resistance against fatigue cracking than other high-energy GBs. From these innovative studies, controlling the GBCD is of great significance for improving the properties related to GBs.

It is well-recognized that optimized GBCDs are usually realized through thermomechanical processing (TMP) of cold/warm rolling with low strain (about 5%) followed by annealing [19–22]. In our previous work [23], by performing systematic hot rolling and quasi in-situ heating observation tests, it was found that the optimized GBCD could also be realized by modifying the processing parameters of hot rolling, which provide a new idea for regulating GBCDs in heavy-gauge nuclear-grade ASSs. However, although deformations of low strain can induce the optimization of GBCDs, they are usually completed during heat treatment. That is, the heat treatment process directly determines the GBCDs of the final products. Michiuchi et al. [24] showed that the high frequency of CSL boundaries (about 86%) could be introduced into type 316 ASS after 3% pre-strain and long-time annealing (72 h at 967 °C). Shimada et al. [25] indicated that through long-time annealing at low temperature in a specimen of slightly pre-strained 304 ASS, an optimum GBCD described as a uniform distribution of high frequency of CSL boundaries and consequent discontinuity of the random boundary network could be formed. Moreover, by performing in situ heating observation of GBCD evolution at 947 °C for 3% cold-rolled 304 ASS, Tokita et al. [26] found that with the extension of annealing time, the frequency of CSL boundaries gradually increased, accompanied by the growth of grain clusters. These enhanced studies demonstrated that annealing at low temperature for a long time is greatly beneficial to the optimization of GBCDs in a microstructure. In addition, some researchers pointed out that multistage TMP treatment can also promote the formation of a high fraction of CSL boundaries or/and modification of their distribution [20,27,28].

For the heavy-gauge plates of nuclear grade ASSs, however, the solution annealing temperature is generally higher (above 1000 °C) for considering the regulation of different hot-rolled microstructures (e.g., dynamic recrystallized and non-recrystallized microstructure [29]) and the prevention of carbide precipitation (especially for the higher carbon ASS [30]). Moreover, due to the high manufacturing cost and difficulty of this kind of product, it is necessary to take into account the microstructure evolution law of the material (such as recrystallization and grain growth behavior) and the production concept of low cost and easy operation in the process of heat treatment. In other words, how to meet the GBCD optimization on the basis of reducing production cost. The main purpose of this work is to elaborate the influence of heat treatment process on the evolution of Σ^{3n} boundaries and their character distribution, and further develop a new control principle of microstructure to realize the optimization of GBCDs in heavy gage ASS worked in harsh environments. Based on this, series solution annealing experiments with different temperature and time were carried out in a hot-rolled nuclear grade 316H plate with low strain, and the GBCDs were analyzed under different conditions.

2. Experimental Procedures

The experimental material was a solution annealed plate of nuclear grade 316H ASS, which has the composition of 0.046 C, 18.0 Cr, 11.8 Ni, 2.7 Mo, 1.5 Mn, 0.41 Si, 0.06 N, 0.014 P, 0.001 S, 0.0002 B, 0.007 Al, 0.02 Co and the balance Fe (weight percent, %) [3]. Initial 316H plate with 12 mm thickness was firstly heated at 800 °C for 20 min to homogenize the heat, then immediately hot-rolled with 5% reduction through one pass and water-quenched to freeze the microstructure. Subsequently, the hot-rolled plate was cut into the same multiple samples and performed solution annealing treatment at 1010 °C and 1060 °C for 0.5 h, 1 h, 2 h, 4 h followed by water quench, respectively, labeled as different specimens for the analysis of GBCDs.

Electron backscattered diffraction (EBSD, HKL/Channel 5) was used to characterize the GBCDs after hot-rolling and solution-annealing treatment. The tested specimens were

electropolished in a mixture of ethanol and perchloric acid (7:1 vol.%) at voltage of 32 V for 25 s for removing surface strained layers, and then detected on a Zeiss Ultra 55 with the step size of 1~2 μm at acceleration voltage of 20 kV. In this study, the GBCDs mainly included the length fraction of $\Sigma 3^n$ ($1 \leq n \leq 3$) boundaries (F_Σ), the size of twin-related grain cluster (L_C) and the extent of connectivity for random high-angle GBs (RHAGBs) characterized by the $J_2/(1 - J_3)$ parameter ('n' refers to a triple junction having n number of CSL boundaries at the intersection) [6,7,31]. The $\Sigma 3^n$ boundaries are defined according to Palumbo–Aust criterion [32], and the RHAGBs are defined as those with misorientation $\theta \geq 15^\circ$ but not low Σ ($\Sigma \leq 29$) CSL boundaries. A twin-related grain cluster can be identified as a region in which all of the GBs within a given cluster of grains are described by a $\Sigma 3^n$ boundary and they are interconnected to each other via the RHAGBs, also known as twin-related domains (TRDs) [3,10,11].

3. Results and Discussion

3.1. Evolution of GBCDs with Different Heat Treatment Processes

Figure 1 shows the microstructure of after hot rolling at 800 $^\circ\text{C}$ with 5% reduction (initial specimen). As can be seen from Figures 1a and 1b, some low-angle GBs (LAGBs, $2^\circ \leq \theta < 15^\circ$, $F_{\text{LAGB}} = 17.5\%$) appeared around the GBs of original grains, presenting a certain residual strain. Meanwhile, the presence of a large number of interconnected RHAGBs in the microstructure indicates that the size of TRDs (L_C) was very small, and the $\Sigma 3^n$ boundaries were distributed independently inside the grains. That is, the GBCDs in hot-rolled samples were not optimized.

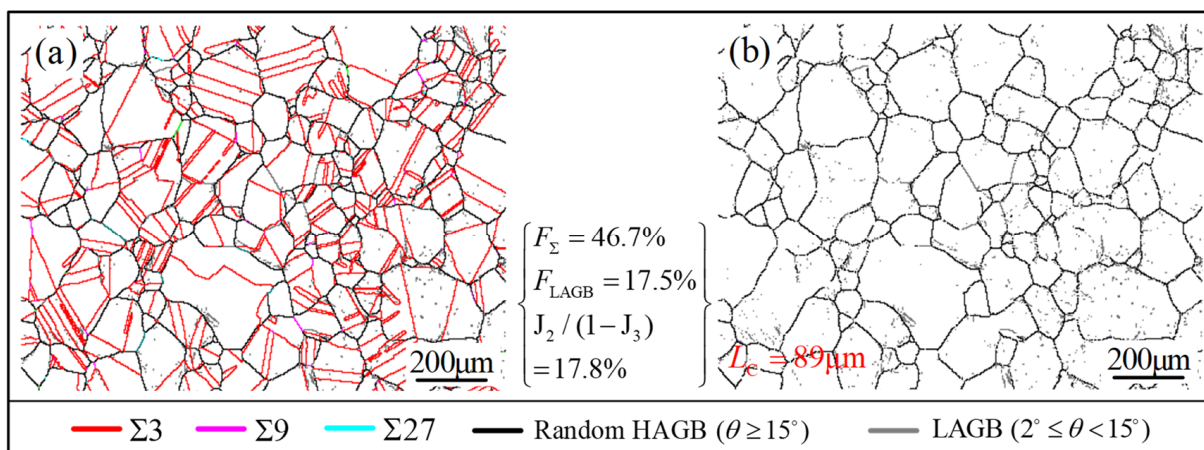


Figure 1. GB distribution map (a) and random GB map (b) of initial specimen (hot rolling at 800 $^\circ\text{C}$ with 5% reduction).

When the abovementioned microstructure was subjected to solution annealing at 1010 $^\circ\text{C}$ and 1060 $^\circ\text{C}$ for different times, the GBCDs presented distinctly different results and evolution rules, as shown in Figures 2 and 3. For the condition of annealing at 1010 $^\circ\text{C}$, after holding for 0.5 h, many TRDs with mixed distribution in size formed in the GB network of being divided by RHAGBs, in which abundant $\Sigma 3^n$ boundaries with different characteristics (including different boundary types and morphology) were distributed, as displayed in Figures 2a and 3a. When the holding time was prolonged from 0.5 h to 4 h, Figures 2c,e,g and 3c,e,g, the number of small-size TRDs decreased obviously with the increase in $\Sigma 3^n$ boundaries and the interruption of the connection network for RHAGBs, and gradually developed into TRDs with larger size and uniform distribution in the GB network, during which the number of $\Sigma 3^n$ boundaries with large length and straight morphology also increased. According to the statistical results of GBCDs, the values of F_Σ , $J_2/(1 - J_3)$ and L_C reached 78.0%, 48.0% and 480 μm , respectively, after holding for 4 h, which was much higher than the corresponding values of 55.3%, 25.6% and 132 μm after

holding for 0.5 h. Moreover, it can be seen from the variation trend in Figures 4 and 5 that both the $J_2/(1 - J_3)$ and L_C values increased rapidly after annealing for 1 h, reaching 38.9% and 388 μm , respectively, and continued to increase slowly with the increase of holding time. The F_Σ value, however, hardly changed after annealing for 1 h.

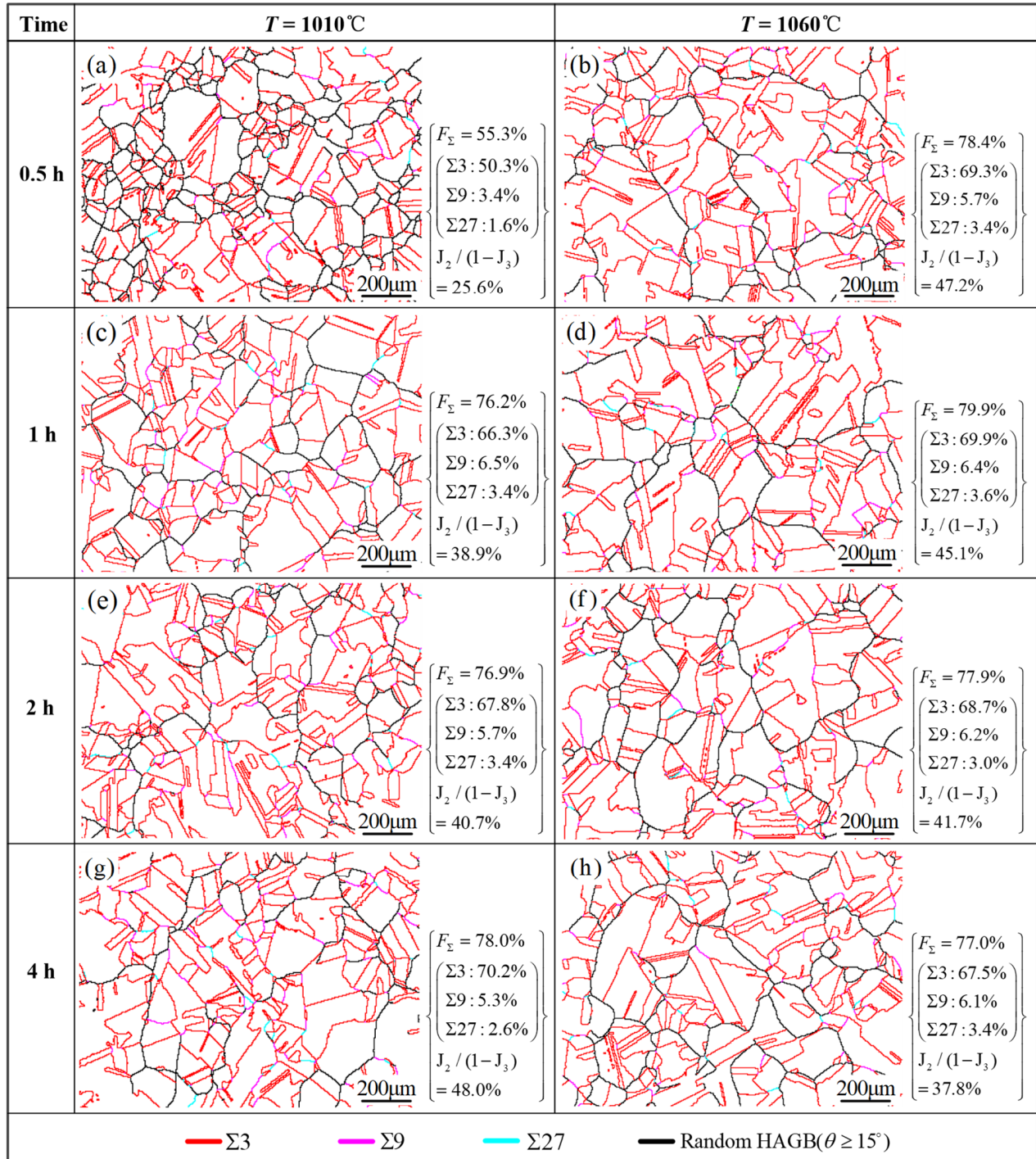


Figure 2. GB distribution maps of specimens annealed at 1010 °C and 1060 °C for different time based on the initial plate after hot-rolling at 800 °C with 5% reduction. (a,c,e,g) 1010 °C vs. 0.5 h, 1 h, 2 h, 4 h; (b,d,f,h) 1060 °C vs. 0.5 h, 1 h, 2 h, 4 h.

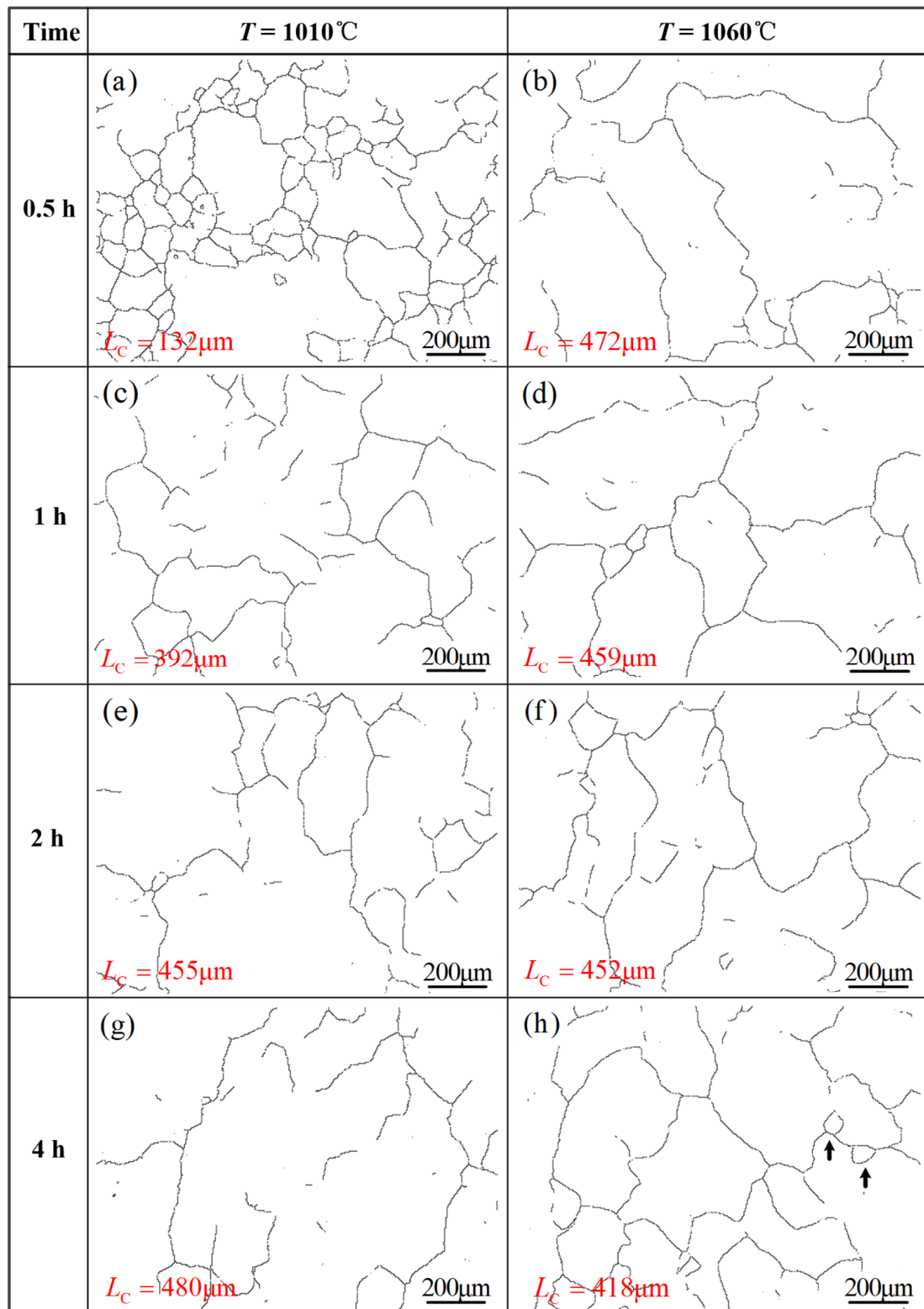


Figure 3. Random GB maps of specimens annealed at 1010°C and 1060°C for different time based on the initial plate after hot-rolling at 800°C with 5% reduction. (a,c,e,g) 1010°C vs. 0.5 h, 1 h, 2 h, 4 h; (b,d,f,h) 1060°C vs. 0.5 h, 1 h, 2 h, 4 h.

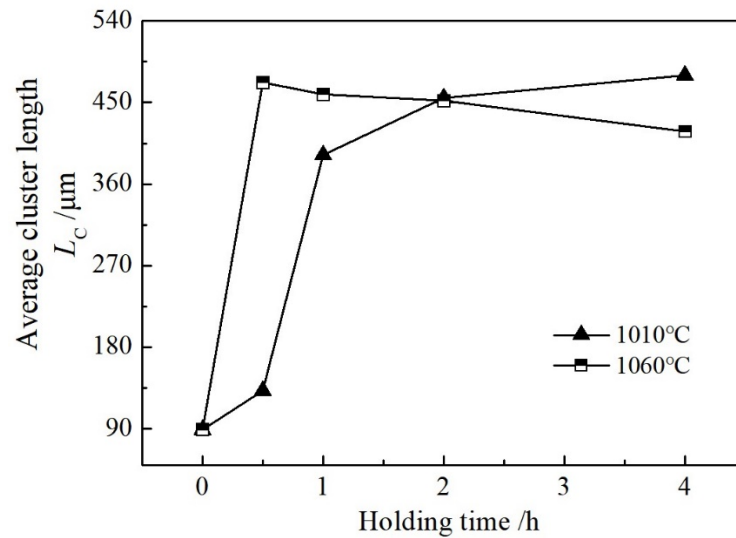


Figure 4. Evolution of the L_C with holding time at different solution annealing temperature.

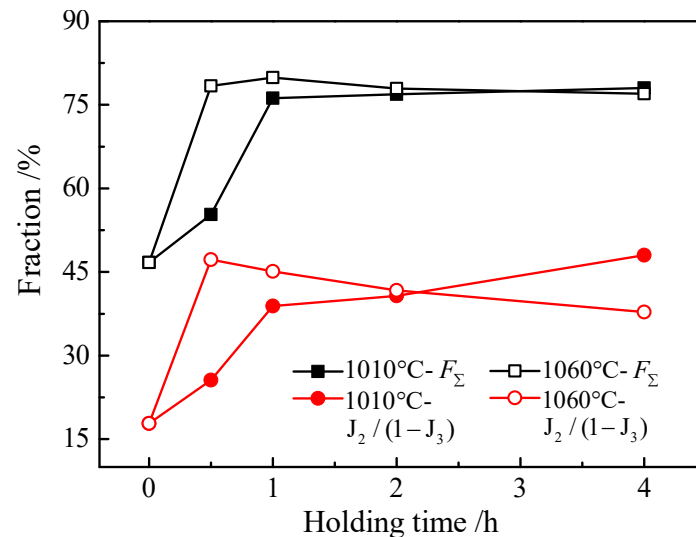


Figure 5. Evolution of the F_Σ and $J_2/(1 - J_3)$ with holding time at different solution annealing temperature.

In contrast, under the solution annealing condition of 1060 °C, the TRDs with relatively uniform distribution (Figure 2b) and large size (472 μm (Figure 3b)) formed after holding for 0.5 h, and the F_Σ and $J_2/(1 - J_3)$ almost reached their maximum values of 78.4% and 47.2%, respectively. These results of GBCDs are all close to the GBCDs after solution annealing at 1010 °C for 4 h. With the increase in holding time, L_C and $J_2/(1 - J_3)$ values decreased slowly, presenting an opposite trend to that of annealing at 1010 °C, as shown in Figures 4 and 5. The F_Σ value, however, gradually stabilized at about 77.0%, which was basically consistent with that annealing at 1010 °C for a long time (Figure 5). From the corresponding microstructure, Figures 2d,f,h and 3d,f,h, it can be seen that in the annealing process of 1–4 h, the TRDs with small size (as indicated by black arrows in Figure 3h) appeared again in local areas, and some interconnected RHAGB formed around them. They reflect that during this process the new recrystallization nucleation has occurred in the local area and promoted the formation of relatively fine grains.

The above observations suggest that recrystallization nucleation and grain growth were easy to occur during solution annealing at higher temperature, which could accelerate the formation of large size TRDs in the microstructure and optimize the GBCDs. However, it is important to note that due to repeated recrystallization nucleation, continuous extension of annealing time at higher temperature would reduce the size of TRDs and the connectivity

of $\Sigma 3^n$ boundaries. On the other hand, by combining the analysis of microstructure and the statistical results of GBCDs under different heat treatment conditions, it can be seen that the length fraction of $\Sigma 3^n$ boundaries (F_Σ) changed very slowly after reaching about 77% at any temperature, i.e., the continuous increase of annealing time had little effect on the fraction (or number) of $\Sigma 3^n$ boundaries. However, in the case of the constant number, increasing the duration at lower temperature could significantly increase the frequency of interconnected $\Sigma 3^n$ boundaries and the size of TRDs (such as the L_C value changing from 392 μm to 480 μm (Figure 3c,e,g)), and dramatically interrupt the topology network of RHAGBs (such as $J_2/(1 - J_3)$, whose value changed from 38.9% to 48.0% (Figure 2c,e,g)). That is, GBCDs in the GB network were optimized.

The operation of GB migration, recrystallization and grain growth during annealing after hot rolling are identified as critical processes for the formation of large TRDs and the optimization of GBCDs [23], among which the low deformation storage energy generated by initial pre-strain first induces multiple twinning events through GB migration and recrystallization during annealing to form abundant $\Sigma 3^n$ boundaries and gradually replace the RHAGBs [22,33–35]. As the new grains grow up and the GB migrates, local $\Sigma 3^n$ boundaries with low-symmetry twin facets and multiple steps (higher interfacial free energy [3,36]) further develop into coherent $\Sigma 3$ twins and interconnected chains in the action of faceting–roughening transition [37,38], by which the remaining topology network of RHAGBs is interrupted and the GBCD is significantly optimized [6,8,25]. In other words, the optimization of GBCDs during heat treatment process mainly goes through two stages: (I) Forming a large number of annealing twins. This process is mainly completed through the transformation of deformation storage energy into the interfacial free energy dominated by the $\Sigma 3^n$ boundaries with higher free energy. (II) Driven by the continuous decrease of free energy, the character distribution of $\Sigma 3^n$ boundaries are continuously optimized, while the topological network of RHAGBs are further interrupted. This process is mainly accomplished by grain growth and GB migration.

For the solution annealing condition of 1010 °C, the low deformation storage energy produced by hot rolling will first promote the GB migration and recrystallization initiation, resulting in the formation of abundant $\Sigma 3^n$ boundaries and local clusters (Figure 1 vs. Figures 2a and 3a). With the grain growth and gradual migration of GBs at longer holding time, the character distribution of $\Sigma 3^n$ boundaries are further optimized to evolve into larger TRDs, and the connection network of RHAGBs is continuously interrupted, presenting increased values of L_C and $J_2/(1 - J_3)$, as shown in Figures 4 and 5. For the length fraction of $\Sigma 3^n$ boundaries (F_Σ), since the increase in $\Sigma 3^n$ mainly occurs in the first stage (I) mentioned above, the extension of holding time has little effect on it, that is, the value of F_Σ changes slightly.

When solution annealing is carried out at higher temperature of 1060 °C, TRDs can be rapidly induced and the GBCDs are optimized. However, since the thermodynamics of recrystallization is significantly increased at high temperature, the recrystallization nucleation occurs more easily in the region of higher interfacial free energy even when the deformation storage energy is not high, which promotes the formation of new fine grains, as shown in Figure 3h. These smaller grains enhance the topological network of RHAGBs, thus reducing the size of TRDs and blocking the further optimization of $\Sigma 3^n$ boundaries. Therefore, the values of L_C and $J_2/(1 - J_3)$ decrease slowly during annealing at this temperature for a long time.

3.2. Proliferation Mechanism of $\Sigma 3^n$ Boundaries during Heat Treatment Process

As displayed in Figures 1a and 2, a significant change in the microstructure after solution annealing is that high proportion of $\Sigma 3^n$ boundaries were obtained, including $\Sigma 3$, $\Sigma 9$ and $\Sigma 27$ boundaries with different morphologies and length fraction (see statistics of $\Sigma 3^n$ boundaries on the right side of corresponding GB distribution map). However, according to the length fraction and morphology of boundaries distinguished by different Σ index, it can be seen that there were differences in the distribution patterns of $\Sigma 3^n$ boundaries for

specimens of annealing at 1010 °C and 1060 °C, which can mainly relate to the proliferation mechanism of $\Sigma 3^n$ boundaries.

Studies indicated that $\Sigma 3^n$ boundaries generate during annealing in the metallic materials with low stacking fault energy and crystal structure of face-centric cubic (FCC) mainly through two ways: (1) New twinning mechanism [34]. This process is accomplished through initial nucleation of stacking faults and the growth accidents in the process of GB migration during recrystallization and grain growth, among which the twins often form on the close-packed plane of GBs and grow with the growth of grains [39,40]. The $\Sigma 3$ twin boundary formed in this way is relatively straight in morphology and long in length, and the coherent interface is parallel to the {111} crystal plane, while the twin steps and twin terminals are non-coherent. (2) $\Sigma 3$ regeneration mechanism [34,35]. This mainly occurs in the process of interfacial migration and integration, in which $\Sigma 3^n$ boundaries proliferate through the interface reaction of CSL boundaries with different Σ index when they meet, such as the reaction of $\Sigma 3^n + \Sigma 3^{n+1} \rightarrow \Sigma 3$ [35] and $\Sigma 3 + \Sigma 3^n \rightarrow \Sigma 3^{n+1}$ [28]. For the $\Sigma 3^n$ boundaries formed in this way, a large number of $\Sigma 9$ and $\Sigma 27$ with complex morphologies can be observed in the GB network, and they usually have high mobility for changing quantity and morphology with interface reaction. In the actual thermomechanical process, both modes may be effective, but one of the mechanisms in play are dominant [41], which is reflected by the ratio of $\Sigma 3/(\Sigma 9 + \Sigma 27)$ ($R_{\Sigma 3/(\Sigma 9 + \Sigma 27)}$). The lower the ratio of $\Sigma 3/(\Sigma 9 + \Sigma 27)$, the more dominant the regeneration mechanism is, where the grain interface has strong mobility and complicated morphology, and easily evolves into a straight shape. When the $\Sigma 3/(\Sigma 9 + \Sigma 27)$ ratio is high, it indicates that a high proportion of $\Sigma 3^n$ boundaries is formed through the new twinning mechanism. In this study, in order to clarify the proliferation behavior of $\Sigma 3^n$ boundaries under different heat treatment conditions, comprehensive analysis including the fraction and morphology characteristics of $\Sigma 3^n$ boundaries with different Σ index, and the ratio of $\Sigma 3/(\Sigma 9 + \Sigma 27)$ were carried out.

Figure 6 shows the variation of length fractions for $\Sigma 3^n$ boundaries ($\Sigma 3$, $\Sigma 9 + \Sigma 27$ and $\Sigma 3/(\Sigma 9 + \Sigma 27)$ ratio) at different annealed specimens. It can be seen that the $F_{\Sigma 3}$ value gradually increased first and then tended to be stable with the extension of holding time at both 1010 °C and 1060 °C, which present the same evolution pattern with the F_{Σ} in Figure 5, demonstrating that $\Sigma 3$ is the main part of $\Sigma 3^n$ boundaries. The values of $F_{\Sigma 9 + \Sigma 27}$ and $R_{\Sigma 3/(\Sigma 9 + \Sigma 27)}$, however, showed different patterns at the two temperatures. For the annealing temperature of 1010 °C, $F_{\Sigma 9 + \Sigma 27}$ first increased to about 9.9% (holding for 1 h) and then slowly decreased, but the change of $R_{\Sigma 3/(\Sigma 9 + \Sigma 27)}$ showed an opposite trend. They reflect that both the new twinning mechanism and $\Sigma 3$ regeneration mechanism contribute to the proliferation of $\Sigma 3^n$ boundaries at the initial stage of annealing, and with increasing annealing time, the new twinning mechanism gradually becomes the dominant mode. Furthermore, it is found from the morphology of $\Sigma 3^n$ boundaries shown in Figure 2 that the $\Sigma 3^n$ boundaries formed at the initial stage of annealing mainly presented a multi-step curved shape and short size, and with the increase in annealing time they gradually adjusted the morphologies for evolving into larger $\Sigma 3$ boundaries and interconnected chains or clusters. Moreover, some $\Sigma 9$, $\Sigma 27$ and RHAGB in the GB network gradually transformed into $\Sigma 3$ boundaries. That is, the GBCDs was further optimized, as demonstrated in Section 3.1.

When the solution annealing temperature was increased to 1060 °C, the values of $F_{\Sigma 9 + \Sigma 27}$ and $R_{\Sigma 3/(\Sigma 9 + \Sigma 27)}$ almost reached their maximum at 0.5 h duration. As annealing time increased, they basically remained at about 9.5% and 7.3%, even though there were some fluctuations. These results indicate that both abovementioned mechanisms facilitated the proliferation of $\Sigma 3^n$ boundaries in this heat treatment process, and they basically maintained the balance with the extension of holding time. Moreover, from the statistical result of $F_{\Sigma 3}$ and $F_{\Sigma 9 + \Sigma 27}$, they were not prone to change in the process of long-time annealing, that is, both the interface reactions of $\Sigma 3^n + \Sigma 3^{n+1} \rightarrow \Sigma 3$ and $\Sigma 3 + \Sigma 3^n \rightarrow \Sigma 3^{n+1}$ existed during the proliferation of $\Sigma 3^n$ boundaries.

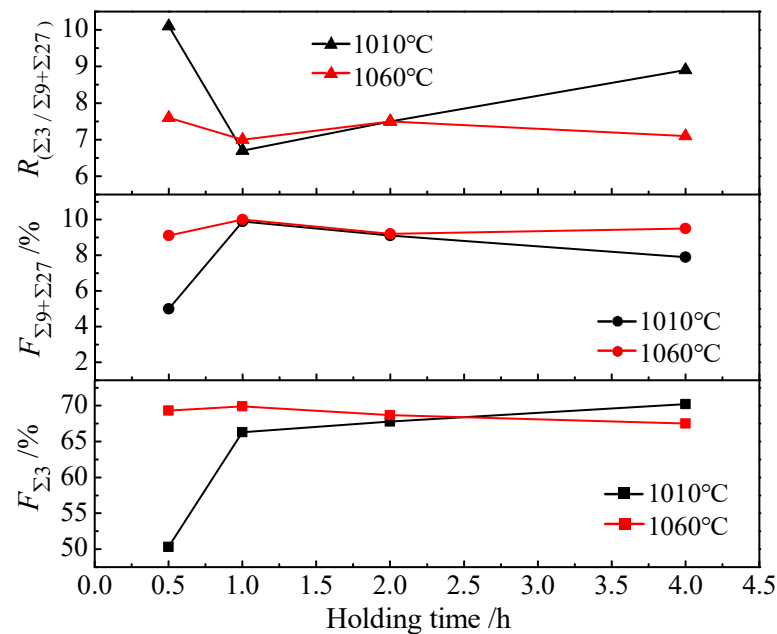


Figure 6. Variation of length fractions for $\Sigma 3^n$ boundaries ($\Sigma 3$, $\Sigma 9 + \Sigma 27$ and $\Sigma 3 / (\Sigma 9 + \Sigma 27)$ ratio) at specimens annealed at 1010 °C and 1060 °C for different times.

4. Conclusions

1. The temperature and holding time during heat treatment process have a significant effect on the GBCDs of hot-rolled 316H ASS for nuclear power. The solution annealing with a long time period at lower temperature or short time period at higher temperature is conducive to obtaining optimized GBCDs, including large TRDs, abundant interconnected $\Sigma 3^n$ boundaries and an interrupted topology network of RHAGBs in the microstructure.
2. The fraction of $\Sigma 3^n$ boundaries has no inevitable proportional relationship with their character distribution. It was worked out that the character distribution of $\Sigma 3^n$ boundaries can be further optimized by modifying the solution annealing process even though their length fraction or number does not increase significantly, which provides an important route for realizing the optimization of GBCDs in special ASSs.
3. It is easier to activate the new twinning mechanism by solution annealing at low temperature for a long time, leading to the formation of $\Sigma 3$ boundaries with straight morphology and larger size. In addition, both the new twinning and $\Sigma 3$ regeneration mechanisms exist in the annealing process for introducing the proliferation of $\Sigma 3^n$ boundaries, and they basically maintain the balance with the increase of annealing time at higher temperature.

Author Contributions: Conceptualization, Z.W., W.Z., F.G. and Z.L.; Methodology, Z.W., A.M. and Z.L.; Formal analysis, Z.W., W.Z., A.M. and J.L.; Resources, C.L. and Z.L.; Data curation, Z.W., W.Z., A.M., J.L., F.G. and C.L.; Writing—original draft, Z.W., W.Z. and F.G.; Writing—review and editing, Z.W. and F.G.; Project administration, Z.L.; Funding acquisition, F.G. and Z.L. All authors have read and agreed to the published version of the manuscript.

Funding: The authors are grateful to the financial supports by the National Key Research and Development Program of China (No. 2017YFB0305002), and the Fundamental Research Funds for the Central Universities (No. N2202021).

Acknowledgments: The authors are grateful to the financial supports by the National Key Research and Development Program of China (No. 2017YFB0305002), and the Fundamental Research Funds for the Central Universities (No. N2202021).

Conflicts of Interest: The authors declare no conflict of interest.

References

1. Kumar, P.; Pai, A. An overview of welding aspects and challenges during manufacture of intermediate heat exchangers for 500mwe prototype fast breeder reactor. *Procedia Eng.* **2014**, *86*, 173–183. [[CrossRef](#)]
2. Lu, S.Y. *Introduction to Stainless Steel*; Chemical Industry Press: Beijing, China, 2013; pp. 89–127.
3. Wang, Z.G.; Gao, F.; Tang, S.; Zhou, P.; Zhang, W.N.; Liu, Z.Y. Effect of twin-related boundaries distribution on carbide precipitation and intergranular corrosion behavior in nuclear-grade higher carbon austenitic stainless steel. *Corros. Sci.* **2022**, *209*, 110791. [[CrossRef](#)]
4. Babu, K.A.; Mozumder, Y.H.; Saha, R. Hot-workability of super-304H exhibiting continuous to discontinuous dynamic recrystallization transition. *Mater. Sci. Eng. A* **2018**, *734*, 269–280. [[CrossRef](#)]
5. Wang, Q.A.; Long, B.; Wang, X.T.; Fang, Y.C.; Zhang, D.H.; Zhou, P.D. Study on research and development system of materials for sodium-cooled fast reactor technology. *J. Iron Steel Res.* **2014**, *26*, 1–6.
6. Tsurekawa, S.; Nakamichi, S.; Watanabe, T. Correlation of grain boundary connectivity with grain boundary character distribution in austenitic stainless steel. *Acta Mater.* **2006**, *54*, 3617–3626. [[CrossRef](#)]
7. Kobayashi, S.; Kobayashi, R.; Watanabe, T. Control of grain boundary connectivity based on fractal analysis for improvement of intergranular corrosion resistance in SUS316L austenitic stainless steel. *Acta Mater.* **2016**, *102*, 397–405. [[CrossRef](#)]
8. Shi, F.; Tian, P.C.; Jia, N.; Ye, Z.H.; Qi, Y.; Liu, C.M.; Li, X.W. Improving intergranular corrosion resistance in a nickel-free and manganese-bearing high-nitrogen austenitic stainless steel through grain boundary character distribution optimization. *Corros. Sci.* **2016**, *107*, 49–59. [[CrossRef](#)]
9. Hu, C.L.; Xia, S.; Li, H.; Liu, T.G.; Zhou, B.X.; Chen, W.J.; Wang, N. Improving the intergranular corrosion resistance of 304 stainless steel by grain boundary network control. *Corros. Sci.* **2011**, *53*, 1880–1886. [[CrossRef](#)]
10. Pradhan, S.K.; Bhuyan, P.; Mandal, S. Individual and synergistic influences of microstructural features on intergranular corrosion behavior in extra-low carbon type 304L austenitic stainless steel. *Corros. Sci.* **2018**, *139*, 319–332. [[CrossRef](#)]
11. Barr, C.M.; Thomas, S.; Hart, J.L.; Harlowe, W.; Anber, E.; Taheri, M.L. Tracking the evolution of intergranular corrosion through twin-related domains in grain boundary networks. *npj Mater. Degrad.* **2018**, *2*, 14. [[CrossRef](#)]
12. Liu, T.G.; Xia, S.; Shoji, T. Intergranular stress corrosion cracking in simulated BWR water of 316L stainless steels manufactured with different procedures. *Corros. Sci.* **2021**, *183*, 109344. [[CrossRef](#)]
13. Rahimi, S.; Marrow, T.J. A new method for predicting susceptibility of austenitic stainless steels to intergranular stress corrosion cracking. *Mater. Design* **2020**, *187*, 108368. [[CrossRef](#)]
14. Bechtle, S.; Kumar, M.; Somerday, B.P.; Launey, M.E.; Ritchie, R.O. Grain-boundary engineering markedly reduces susceptibility to intergranular hydrogen embrittlement in metallic materials. *Acta Mater.* **2009**, *57*, 4148–4157. [[CrossRef](#)]
15. Alyousif, O.M.; Rokuro, N. On the stress corrosion cracking and hydrogen embrittlement behavior of austenitic stainless steels in boiling saturated magnesium chloride solutions. *Int. J. Corros.* **2012**, *2012*, 462945. [[CrossRef](#)]
16. Kobayashi, S.; Maruyama, T.; Saito, S.; Tsurekawa, S.; Watanabe, T. In situ observations of crack propagation and role of grain boundary microstructure in nickel embrittled by sulfur. *J. Mater. Sci.* **2014**, *49*, 4007–4017. [[CrossRef](#)]
17. Li, L.L.; Zhang, Z.J.; Zhang, P.; Zhang, Z.F. Higher fatigue cracking resistance of twin boundaries than grain boundaries in Cu bicrystals. *Scr. Mater.* **2011**, *65*, 505–508. [[CrossRef](#)]
18. Li, L.L.; Zhang, Z.J.; Zhang, P.; Wang, Z.G.; Zhang, Z.F. Controllable fatigue cracking mechanisms of copper bicrystals with a coherent twin boundary. *Nat. Commun.* **2014**, *5*, 3536. [[CrossRef](#)]
19. Xia, S.; Zhou, B.X.; Chen, W.J.; Wang, W.G. Effects of strain and annealing processes on the distribution of $\Sigma 3$ boundaries in a Ni-based superalloy. *Scr. Mater.* **2006**, *54*, 2019–2022. [[CrossRef](#)]
20. Engelberg, D.L.; Newman, R.C.; Marrow, T.J. Effect of thermomechanical process history on grain boundary control in an austenitic stainless steel. *Scr. Mater.* **2008**, *59*, 554–557. [[CrossRef](#)]
21. Barr, C.M.; Leff, A.C.; Demott, R.W.; Doherty, R.D.; Taheri, M.L. Unraveling the origin of twin related domains and grain boundary evolution during grain boundary engineering. *Acta Mater.* **2018**, *144*, 281–291. [[CrossRef](#)]
22. Liu, T.G.; Xia, S.; Du, D.H.; Bai, Q.; Zhang, L.F.; Lu, Y.H. Grain boundary engineering of large-size 316 stainless steel via warm-rolling for improving resistance to intergranular attack. *Mater. Lett.* **2019**, *234*, 201–204. [[CrossRef](#)]
23. Wang, Z.G.; Tang, S.; Zhang, W.N.; Gao, F.; Chen, J.; Liu, Z.Y. Induction of large twin related domains and the grain boundary evolution during hot plate rolling and annealing of 316H-type stainless steel. *Mater. Lett.* **2022**, *311*, 131590. [[CrossRef](#)]
24. Michiuchi, M.; Kokawa, H.; Wang, Z.J.; Sato, Y.S.; Sakai, K. Twin-induced grain boundary engineering for 316 austenitic stainless steel. *Acta Mater.* **2006**, *54*, 5179–5184. [[CrossRef](#)]
25. Shimada, M.; Kokawa, H.; Wang, Z.J.; Sato, Y.S.; Karibe, I. Optimization of grain boundary character distribution for intergranular corrosion resistant 304 stainless steel by twin-induced grain boundary engineering. *Acta Mater.* **2002**, *50*, 2331–2341. [[CrossRef](#)]
26. Tokita, S.; Kokawa, H.; Sato, Y.S.; Fujii, H.T. In situ EBSD observation of grain boundary character distribution evolution during thermomechanical process used for grain boundary engineering of 304 austenitic stainless steel. *Mater. Charact.* **2017**, *131*, 31–38. [[CrossRef](#)]
27. Owen, G.; Randle, V. On the role of iterative processing in grain boundary engineering. *Scr. Mater.* **2006**, *55*, 959–962. [[CrossRef](#)]
28. Zhang, M.X. *Study on the Intergranular Corrosion and the Optimization of Grain Boundary Character Distribution of 316L(N) Austenitic Stainless Steel*; University of Science and Technology Beijing: Beijing, China, 2017.

29. Wang, Z.G.; Gao, F.; Zhang, W.N.; Cao, G.M.; Liu, Z.Y. Transitional behavior for dynamic recrystallization in nuclear grade 316H stainless steel during hot deformation. *Metall. Mater. Trans. A* **2022**, *53*, 523–534. [[CrossRef](#)]
30. Wang, Z.G.; Gao, F.; Cao, G.M.; Tang, S.; Liu, Z.Y. Elemental inter-diffusions for the transformation of $\delta/M_{23}C_6/\gamma$ phases during heat treatment processes in heavy gage 316H-type austenitic stainless steel. *Metall. Mater. Trans. A* **2022**, *53*, 2652–2664. [[CrossRef](#)]
31. Fortier, P.; Miller, W.; Aust, K. Triple junction and grain boundary character distributions in metallic materials. *Acta Mater.* **1997**, *45*, 3459–3467. [[CrossRef](#)]
32. Palumbo, G.; Aus, K.T.; Lehockey, E.M.; Erb, U.; Lin, P. On a more restrictive geometric criterion for “special” CSL grain boundaries. *Scr. Mater.* **1998**, *38*, 1685–1690. [[CrossRef](#)]
33. Liu, T.G.; Xia, S.; Ru, X.K.; Bai, Q.; Zhou, B.X.; Lu, Y.H. Twins and twin-related domains in a grain boundary-engineered 304 stainless steel. *Mater. Sci. Tech.* **2018**, *34*, 561–571. [[CrossRef](#)]
34. Randle, V.; Owen, G. Mechanisms of grain boundary engineering. *Acta Mater.* **2006**, *54*, 1777–1783. [[CrossRef](#)]
35. Randle, V. Mechanism of twinning-induced grain boundary engineering in low stacking-fault energy materials. *Acta Mater.* **1999**, *47*, 4187–4196. [[CrossRef](#)]
36. Olmsted, D.L.; Holm, E.A.; Foiles, S.M. Survey of computed grain boundary properties in face-centered cubic metals: I. Grain boundary energy. *Acta Mater.* **2009**, *57*, 3704–3713. [[CrossRef](#)]
37. Straumal, B.B.; Kogtenkova, O.A.; Gornakova, A.S.; Sursaeva, V.G.; Baretzky, B. Review: Grain boundary faceting-roughening phenomena. *J. Mater. Sci.* **2016**, *51*, 382–404. [[CrossRef](#)]
38. Straumal, B.B.; Baretzky, B.; Kogtenkova, O.A.; Gornakova, A.S.; Sursaeva, V.G. Faceting-roughening of twin grain boundaries. *J. Mater. Sci.* **2012**, *47*, 1641–1646. [[CrossRef](#)]
39. Mahajan, S.; Pande, C.S.; Imam, M.A.; Rath, B.B. Formation of annealing twins in f.c.c. crystals. *Acta Mater.* **1997**, *45*, 2633–2638. [[CrossRef](#)]
40. Na, Y.S.; Yeom, J.T.; Park, N.K.; Lee, J.Y. Electron backscatter diffraction analysis of dynamically recrystallized grain structures in a Ni-Cr-Fe base alloy. *Metall. Mater. Trans. A* **2006**, *37*, 41–47. [[CrossRef](#)]
41. Randle, V. Twinning-related grain boundary engineering. *Acta Mater.* **2004**, *52*, 4067–4081. [[CrossRef](#)]

Disclaimer/Publisher’s Note: The statements, opinions and data contained in all publications are solely those of the individual author(s) and contributor(s) and not of MDPI and/or the editor(s). MDPI and/or the editor(s) disclaim responsibility for any injury to people or property resulting from any ideas, methods, instructions or products referred to in the content.